

# CHAPTER 1

## The NOvA experiment

The NuMI Off-axis  $\nu_e$  Appearance (NOvA) [1] is a long-baseline neutrino oscillation experiment based at the Fermi National Accelerator Laboratory (FERMILAB) [2]. NOvA receives an off-axis  $\nu_\mu$  and  $\bar{\nu}_\mu$  beam from FERMILAB’s Neutrinos from the Main Injector (NuMI) neutrino source (Sec. 1.1) and measures the  $\nu_e$  or  $\bar{\nu}_e$  appearance and the  $\nu_\mu$  or  $\bar{\nu}_\mu$  disappearance between its two highly active and finely segmented detectors (Sec. 1.4) [3].

The capability to measure both the  $\nu_e$  and the  $\bar{\nu}_e$  appearance, coupled with a significant matter effect induced by its long baseline, allows NOvA to address some of the most important questions in neutrino physics to date, such as the neutrino mass ordering, the octant of  $\theta_{23}$ , and the possible Charge conjugation - Parity (CP) symmetry violation in the neutrino sector [3–7]. NOvA data also enables measurements of  $\theta_{13}$ ,  $\theta_{23}$  and  $|\Delta m_{32}^2|$  [3], measurements of neutrino differential cross sections in the Near Detector (ND) [8–11], constraints on the possible sterile neutrino models [12, 13], monitoring for supernova neutrino activity [14, 15], searches for magnetic monopoles [16], or constraints on the neutrino electromagnetic properties (this thesis). Using two functionally identical detectors mitigates the dominant systematic uncertainties of neutrino oscillation measurements, described in Sec. 1.8.

NOvA started taking data in February 2014 and is expected to run through 2026 [17], or until FERMILAB begins redirecting its efforts towards the startup of the upcoming Deep Underground Neutrino Experiment (DUNE) experiment [18].

### 1.1 The Neutrino Beam

The neutrino beam for NOvA comes from the FERMILAB-based NuMI neutrino source [19]. The schematic description of NuMI is shown in Fig. 1.1, starting on the left hand side with 120 GeV protons from the Main Injector (MI), part of the FERMILAB accel-

erator complex. The proton beam is divided into  $10\ \mu\text{s}$  long pulses, with  $\sim 5 \times 10^{13}$  Protons On Target (POT) per spill every  $\sim 1.3\ \text{s}$  long cycle time, resulting in a proton beam power of  $\sim 800\ \text{kW}$  (current record  $959\ \text{kW}$  [20]), with upgrades currently underway to surpass  $1\ \text{MW}$  [21].

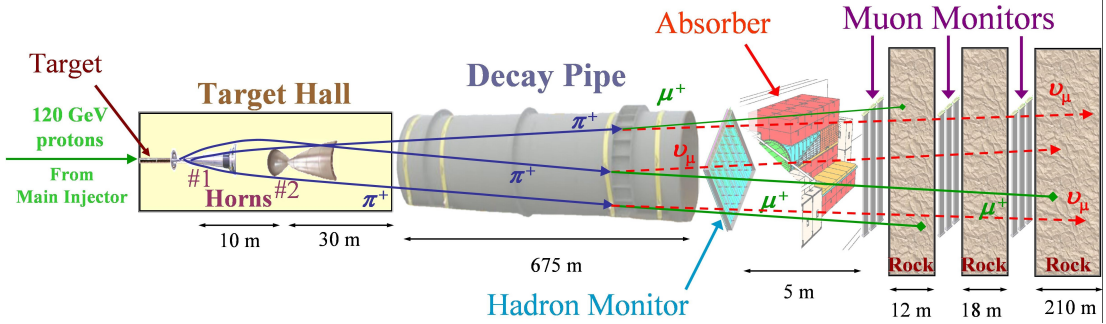


Figure 1.1: The NuMI neutrino beam starts on the left hand side with protons from the MI impinged on a graphite target producing mainly pions and kaons. These are then focused and charge-selected by two focusing horns, after which they decay inside the decay pipe into a high-purity  $\nu_\mu$  or  $\bar{\nu}_\mu$  beam. The residual hadrons are stopped and monitored in the hadron absorber and the remaining muons are recorded with muon monitors and absorbed inside the rock. Figure from [19].

The proton beam passes through a collimating baffle before hitting a  $\sim 1.2\ \text{m}$ -long (equal to about two interaction lengths) graphite target [22], producing hadrons, predominantly pions and kaons [19]. These are then focused and selected by two parabolic magnetic ‘horns’. The focused hadrons pass through a 675 m-long decay pipe filled with helium to create a low density environment for hadrons to propagate and decay in flight into either neutrinos or antineutrinos. High energy hadrons that do not decay in the decay pipe are absorbed within a massive aluminium, steel, and concrete hadron absorber and monitored with a hadron monitor. The leftover muons are ranged out in dolomite rock after the absorber and monitored using three muon monitors. The hadron and muon monitors are ionization chambers, used to monitor the quality, location and relative intensity of the beam.

Using a positive current inside the horns focuses positively charged particles, which then decay into neutrinos, and removes negatively charged particles. Reversing the horn current focuses negatively charged particles, which decay into antineutrinos, and defocuses positively charged particles. The neutrino mode is therefore called Forward Horn Current (FHC) and the antineutrino mode is called Reverse Horn Current (RHC). The composition of the neutrino beam for both these modes

at the **NOvA ND** is shown in Fig. 1.2, displaying the very high purity of the  $\nu_\mu$  or  $\bar{\nu}_\mu$  component in the **FHC** ro **RHC** beam respectively [19].

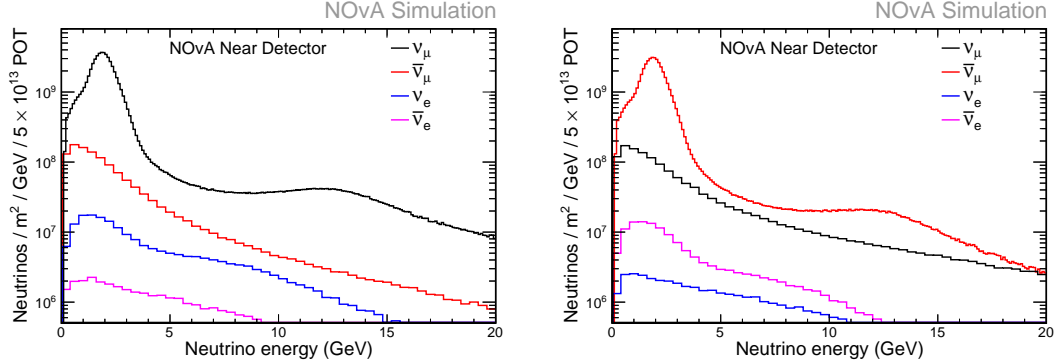


Figure 1.2: The components of the neutrino beam at the **NOvA ND** per one **NuMI** spill in the **FHC** regime shown on the left and the **RHC** regime on the right. The  $\nu_\mu$  ( $\bar{\nu}_\mu$ ) composition in the **FHC** (**RHC**) regime is 93.8% (92.5%), with a wrong sign contribution of 5.3% (6.6%) and only 0.9% (0.9%) contamination by  $\nu_e$  ( $\bar{\nu}_e$ ), showing the high purity of  $\nu_\mu$  and  $\bar{\nu}_\mu$  in the neutrino beam for **NOvA**. Beam composition values calculated for neutrinos with energies between 1 – 5 GeV. Figures are from internal **NOvA** repository [23].

The resulting neutrino beam energy distribution is peaked at  $\sim 7$  GeV with a wide energy band. However, thanks to the kinematics of the dominant pion decay, by placing the **NOvA ND** and Far Detector (FD) 14.6 mrad ( $\approx 0.8^\circ$ ) off the main **NuMI** beam axis, **NOvA** achieves a narrow band neutrino flux peaked at 1.8 GeV [7, 24], as can be seen in Fig. 1.3. Using an off-axis neutrino flux increases the neutrino beam around 2 GeV about 5-fold compared to the on-axis flux and narrow-band peak enhances background rejection for the  $\nu_e$  appearance analysis [24].

## 1.2 The NOvA Detectors

The two main **NOvA** detectors are the **ND**, located in **FERMILAB**  $\sim 1$  km from the **NuMI** target and  $\sim 100$  m under ground, and the **FD**, located  $\sim 810$  km from **FERMILAB** at Ash River in north Minnesota, partially underground with a rock overburden [24]. **NOvA** also operated a detector prototype called Near Detector on the Surface (NDOS), which was used for early research and development of detector components and analysis [4]. Additionally, **NOvA** operated a Test Beam detector, described in detail in Sec. ???. The scales of the **ND** and **FD** are shown in Fig. 1.4.

All **NOvA** detectors are highly segmented, highly active, functionally identical

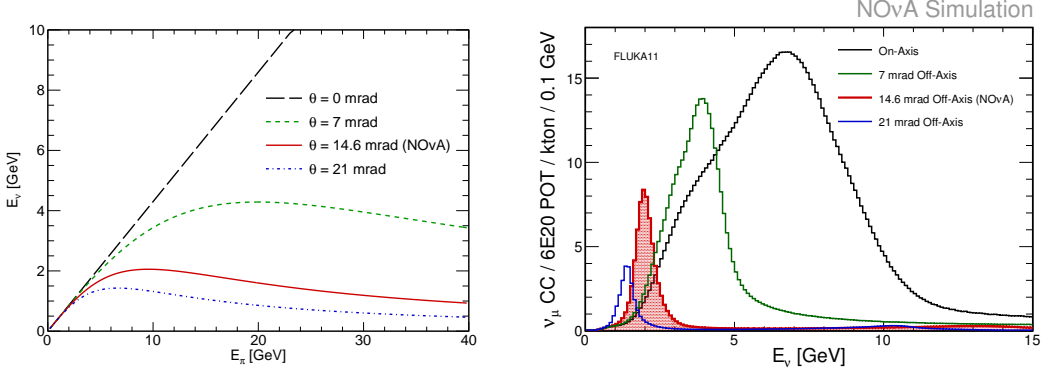


Figure 1.3: (Left) Dependence of the neutrino energy on the parent pion’s energy and (right) neutrino energy distribution for an on-axis beam and three different off-axis beam designs. The case for **NOvA** is shown in red and results in a narrow neutrino energy distribution around 2 GeV, with limited dependence on the parent pion’s energy. Figure from [24]

tracking calorimeters made up of Polyvinyl chloride (PVC) cells filled with liquid scintillator. Each cell is a long rectangular cuboid with depth of 5.9 cm and width of 3.8 cm (with some variations), with cell length extending to the full width/height of each detector, which is  $\sim 4.1$  m for the **ND** and  $\sim 15.6$  m for the **FD** [24]. An example of a **FD** cell is shown on the right of Fig. 1.4.

Cells are connected side-by-side into a 16 cell-wide extrusions with 3.3 mm-wide walls between cells and 4.9 mm-wide walls on the outsides of the extrusions. The first and last cell of each extrusion are  $\sim 3$  mm narrower than the rest of the cells. Two extrusions are connected side-by-side to form a 32 cell-wide module, with each module having a separate readout (see Sec. 1.3). In the **FD**, 12 modules are connected side-by-side to form one plane of the detector. In the **ND** only 3 modules make up a plane. Planes are positioned one after another, alternating between vertical and horizontal orientation, and grouped into diblocks, each containing 64 planes. The **FD** contains 14 diblocks, totalling 896 planes, whereas the **ND** contains 3 diblocks totalling 192 planes. The **ND** also contains a Muon Catcher region, positioned right after the active region, consisting of 22 planes of the normal **NOvA** detector design, 2 modules high and 3 modules wide, sandwiched with 10 steel plates to help range out muons mainly from the  $\nu_\mu$  charged current interactions [4, 24].

The **NOvA** coordinate system is centred with  $(0, 0, 0)$  in the centre of the first plane, relative to the beam direction. The x axis runs from left to right when facing the detector, y axis from bottom to top and z axis runs perpendicular to the planes

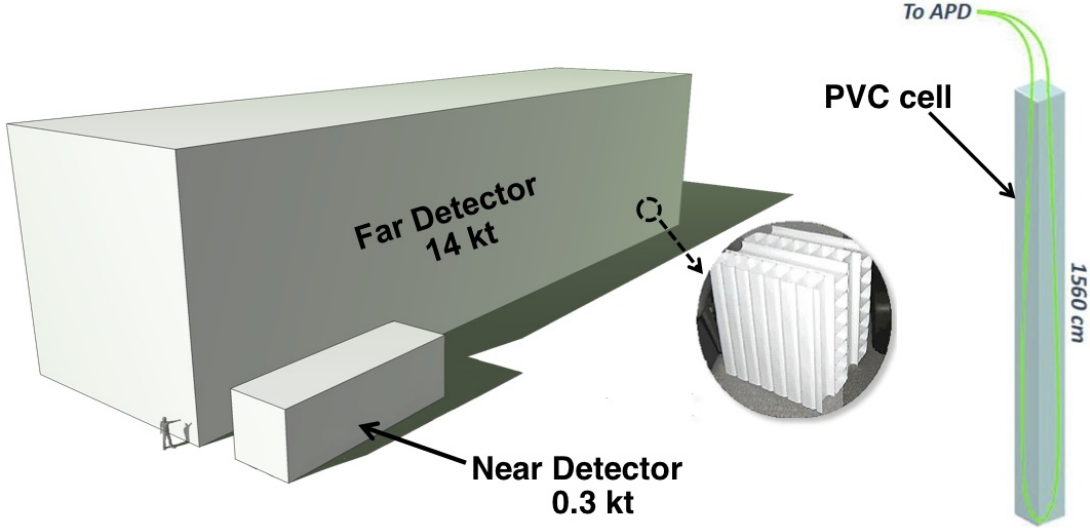


Figure 1.4: Schematic description of the scale and composition of the [NOvA ND](#) and [FD](#). The inset shows a photo of the orthogonal planes made out of [PVC](#) cells. An example of a [FD](#) cell containing liquid scintillator and a looped [WLS](#) fibre attached to an [APD](#) is shown on the right [25].

along the beam direction.

Each cell is filled with a liquid scintillator consisting of mineral oil with 4.1% pseudocumene as the scintillant [26]. Each cell contains a single wavelength shifting fibre with double the length of the cell, looping at one end and connecting to the readout at the other. The [PVC](#) walls of the cells are loaded with highly reflective titanium dioxide, with light typically bouncing off the [PVC](#) walls  $\sim 8$  times before being captured by the Wavelength Shifting (WLS) fibre [24].

The final dimensions of the [FD](#) are  $15.6\text{ m} \times 15.6\text{ m} \times 60\text{ m}$  with a total mass of 14 kT and for the [ND](#) the dimensions are  $3.8\text{ m} \times 3.8\text{ m} \times 12.8\text{ m}$  with a mass of about 0.3 kT [17]. The active volume, consisting only of the liquid scintillator without the [PVC](#) structure, makes up about 70% of the total detector volume [24].

The [NOvA](#) detectors are specifically designed for electromagnetic shower identification, with a radiation length of 38 cm, which amounts to  $\sim 7$  planes for particles travelling perpendicular to the detector planes [4]. This is particularly useful to distinguish electrons from  $\pi^0$ s.

We can calculate the minimum energy an electron needs to have to cross one cell (5.9 cm) of the [NOvA](#) detector by using the measured scintillator density  $0.86\text{ g/cm}^3$  [27] and the electron range [28] in the continuous slowing down approximation in a Polyethylene (approximation of the [NOvA](#) scintillator [29]), as  $E_e \gtrsim 15\text{ MeV}$ .

### 1.3 Readout and Data Acquisition

The signal from the [WLS](#) fibres is read out by an Avalanche Photodiode (APD), converting the scintillation light into electrical signal, with a high quantum efficiency of  $\sim 85\%$  and a gain of 100 [24]. An example [APD](#) is shown in Fig. 1.5. Both ends of each fibre correspond to a single readout channel and are connected to one of the 32 pixels on the [APD](#), with each [APD](#) reading out signal from one module. To maximise the signal to noise ratio, the [APDs](#) are cooled to  $-15^{\circ}\text{C}$  by a thermoelectric cooler, with heat carried away by a water cooling system.

The combination of the [APD](#) quantum efficiency and the light yield, determined by the [PVC](#) reflectivity and the scintillator and [WLS](#) fibre responses, result in a signal requirement of at least 20 Photo Electron (PE) in response to minimum ionizing radiation at the far end of the [FD](#) cell.

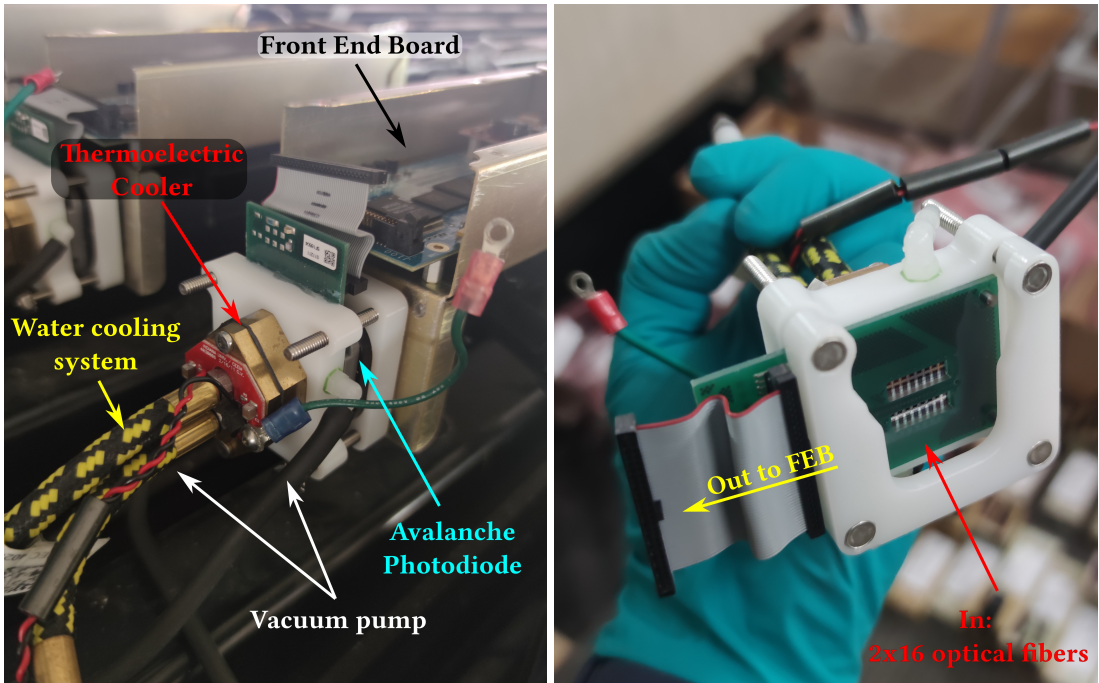


Figure 1.5: The modules with [APD](#)s for [NOvA](#) mounted on top of the detector on the left picture, and shown from the bottom on the right. The individual components of the module are described. The left picture shows a disconnected ribbon cable and ground cable, which are normally connected to the front end board.

Each [APD](#) is connected to a single Front End Board (FEB), shown in Fig. 1.6. The [FEB](#) amplifies and integrates the [APD](#) signal, determines its amplitude and arrival time, before passing it to the Data Acquisition (DAQ) system. On the [FEB](#) the [APD](#) signal is first passed to a custom [NOvA](#) Application-Specific Integrated Circuit (ASIC),

which is designed to maximize the detector sensitivity to small signals. **ASICs** amplify, shape and combine the signal, before sending it to an Analog-to-Digital Converter (ADC). The combined noise from the **APD** and the amplifier is equivalent to about 4 **PEs**, which, compared to an average **PE** yield from the far end of the **FD** cell of 30, results in a good signal and noise separation [24]. The digitized data from an **ADC** is sent to a Field Programmable Gate Array (FPGA), which extracts the time and amplitude of the **ADC** signals, while subtracting noise based on a settable threshold. The **FPGAs** employ multiple correlated sampling methods to reduce noise and improve time resolution of the signal [30].

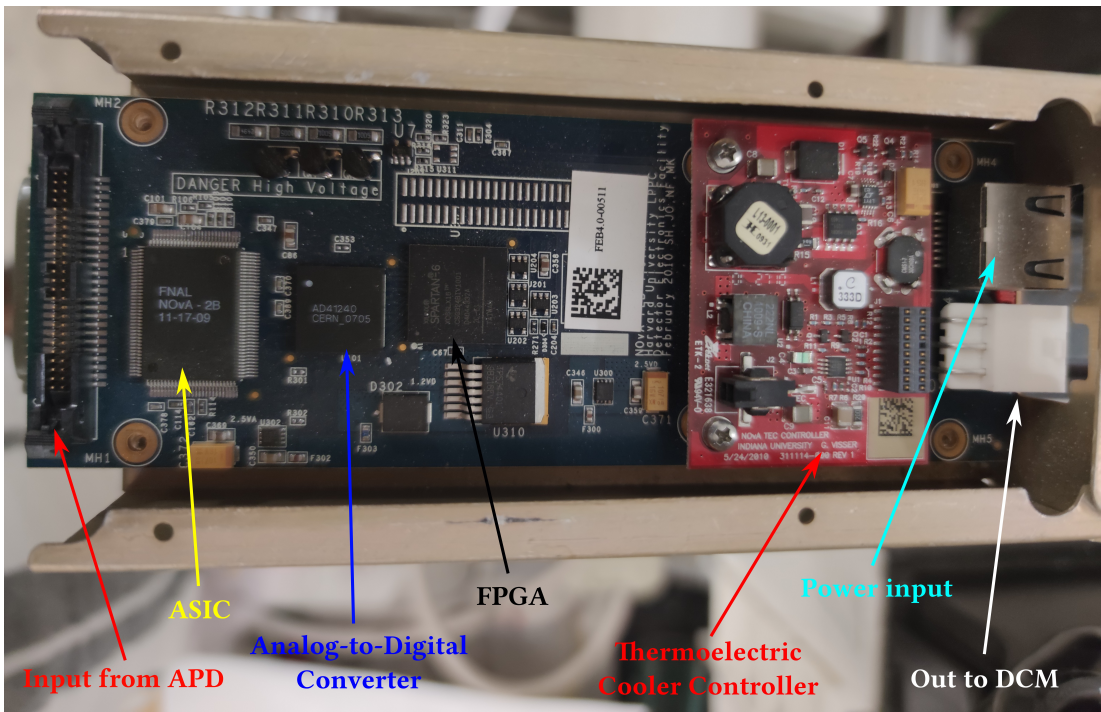


Figure 1.6: An example of a **NOvA FEB** with individual components labelled.

All of the **NOvA** front end electronics (**APDs** and **FEBs**) are operated in a continuous readout mode, without requiring any external triggers [24]. Due to higher detector activity during beam spills, the **ND FEBs** work at a higher frequency of 8 MHz, whereas the **FD FEBs** suffice with 2 MHz sampling frequency [30].

Data from up to 64 **FEBs** are concentrated in a Data Concentration Module (DCM), which concatenates and packages the data into 5 ms time slices, before sending it to the buffer nodes. **DCMs** are also connected to the timing system and pass a single unified timing measurement to the **FEBs** to maintain synchronization across the detector [30].

The buffer nodes cache the data for at least 20 seconds while receiving information from the trigger system. Each trigger uses a time window based either on the time of the [NuMI](#) beam spill, on a periodic interval for monitoring and for the readout of cosmic events, or on one of the activity-based data-driven triggers [30]. Data that fall within any of the trigger windows are sent to a data logger system, where they are merged to form events, before being written to files for offline processing and sent to an online monitoring system. Files are organized based on a unique combination of run and subrun numbers, with runs corresponding to data taking periods with constant detector conditions and limited to either 64 subruns or 24 hours. Subruns are delineated either by a 2 GB file size constraint or a 1-hour timeout limit [31].

The detectors are continuously monitored to ensure data stability and quality. Subruns with suboptimal detector conditions or with events failing basic quality criteria are flagged as ‘bad’ and recorded in a ‘bad runs list’ [31]. Additionally, individual readout channel are assessed on a per-subrun basis, with those with too high or too low hit rates marked as ‘bad’ [32]. Both the ‘good runs’ list and the ‘bad channel’ maps are used to inform event processing and during simulation to emulate real detector conditions.

## 1.4 Simulation

To extract neutrino oscillation parameters, or to test a hypothesis, [NOvA](#) uses a series of simulations to make predictions according to various physical models [33]. The simulation chain can be divided into four parts: simulation of the neutrino beam, simulation of neutrino interactions within the [NOvA](#) detectors, simulation of cosmic particles interacting in the [NOvA](#) detector and simulation of the detector and readout response.

To simulate the neutrino beam, [NOvA](#) uses a simulation based on the GEANT4 v9.2.p03 [34] Monte Carlo (MC) event generator with a detailed model of the [NuMI](#) beamline [35], as described in Sec. 1.4. The simulation starts with the 120 GeV/c [MI](#) protons interacting within the long carbon target and producing hadrons, mainly  $\pi$ ,  $K$  and secondary protons. This is followed by transport and possible further interaction of hadrons within the focusing system, until finally ending with hadron decays

producing the neutrino beam.

To account for the inherently imprecise theoretical models used in GEANT4, **NOvA** uses the Package to Predict the Flux (PPFX) to incorporate external measurements of yields and cross sections of hadron interactions inside the target and the other **NuMI** materials into the neutrino beam prediction [36]. The current version of **PPFX** is limited by the results available during its creation and only corrects the most frequent interactions while assigning conservative systematic uncertainties to the rest (see Sec. 1.8). For the most common  $\pi$ ,  $K$  and  $p$  production, **PPFX** uses the NA49 measurements [37–39] of 158 GeV/c protons interacting on a thin (few percent of interaction length) carbon target. To expand the kinematic coverage, **PPFX** uses a few data points from Barton et al [40] for the  $\pi$  production and  $K/\pi$  ratios from the Main Injector Particle Production (MIPP) [41] experiment for the production of  $K$ . These results have to be scaled to the 20 – 120 GeV/c incident proton moment seen throughout **NuMI** using the FLUKA [42, 43] **MC** generator.

There are two new experiments that measure the production and interaction of hadrons on various targets and incident energies, specifically designed to improve the prediction of neutrino beams. The most impactful measurements from the NA61 experiment are of the 120 GeV/c protons on a thin carbon target [44–46], of the hadron incident interactions [47], and of the 120 GeV/c protons on a **NuMI** replica target [48]. The **FERMILAB**-based EMPHATIC experiment [49] is currently analysing a broad range of hadron production and secondary and tertiary interaction measurements for neutrino beam prediction with a significant involvement of **NOvA** and **DUNE** collaborators.

The output of the neutrino beam simulation is passed to the simulation of neutrino interactions inside the detectors, which is done with the GENIE v3.0.6 [50] neutrino **MC** generator. GENIE allows users to choose the particular models for different types of neutrino interactions and particle propagation within the nucleus, as well as possible tunes to external measurements. The four main interaction modes in GENIE are the Quasi Elastic (QE) Charged current (CC) scattering, the Resonant baryon production (RES), the Deep Inelastic Scattering (DIS), and the Coherent pion production (COH $\pi$ ). The special case of the two particle - two hole (2P2H) interaction via Meson Exchange Current (MEC) and the Final State Interaction (FSI) inside the nucleus are

also considered. The initial state of the nucleus is represented by a local Fermi gas in the **QE** and **2p2h** models, while a global relativistic Fermi gas is used for all other processes. All of these are set by the Comprehensive Model Configuration (CMC), which is currently **N1810j0000** for **NOvA**. Additionally, **NOvA** adds a costume tune to the **NOvA**  $\nu_\mu$ **CC** data for a better constraint of the **CCMEC** interactions. **NOvA** also uses a set of external  $\pi$  interaction measurements to constrain the **FSI** model. Table 1.1 shows the list of models and tunes for different interaction modes in **NOvA** [7].

Table 1.1: Models and tunes used in the **NOvA** simulation of neutrino interactions.

| Interaction                          | Model                       | Tune                                 |
|--------------------------------------|-----------------------------|--------------------------------------|
| <b>CCQE</b>                          | València [51]               | External $\nu - D$ data [52]         |
| <b>CCMEC</b>                         | València [53, 54]           | <b>NOvA</b> $\nu_\mu$ <b>CC</b> data |
| <b>RES &amp; COH<math>\pi</math></b> | Berger-Sehgal [55, 56]      | External $\nu - A$ data              |
| <b>DIS</b>                           | Bodek-Yang [57, 58]         | External $\nu - A$ data              |
| <b>FSI</b>                           | Semi-classical cascade [59] | External $\pi -^{12}C$ data          |

Since the **FD** is on the surface **NOvA** also uses a simulation of cosmic rays generated with the **MC** Cosmic-Ray Shower Generator (CRY) [60]. The simulated cosmic muons are also used to calibrate **NOvA** detectors [36].

Particles that are created from neutrino interactions and cosmic rays are propagated through the **NOvA** detectors using the GEANT4 v10.4.p02 [34], which outputs the energy deposited in the scintillator. This is then passed to a custom **NOvA** simulation software [36], which calculates the amount of scintillation light produced for the deposited energy based on a Poisson distribution. The scintillation light production is parametrized using the Birks-Chou model [61], which corrects for the recombination in organic scintillators at high deposited energies. The scintillator light yield and the inherent production of the Cherenkov light, which can affect the light readout, are tuned to **NOvA** data [9]. The light collection by the **WLS** fibres, its transport to the **APDs**, and the **APD** response use a parametrized simulation, as the **NOvA** cells and their readout are generally the same across the detectors [36]. The simulation of the readout electronics is done by another custom **NOvA** parametrized model, which accounts for random noise in the readout electronics and outputs true events in the same format as the real data.

Due to the high neutrino rate in the **ND**, there are neutrinos interacting in the

surrounding rock creating particles, mainly muons, that make it to the detector and act as background. However, since only a few ‘rock muons’ make it into the detector, it would be very time consuming to run a simulation which includes the rock around the **ND** for every neutrino. Instead, **NOvA** creates a separate simulation that includes the surrounding rock and then overlays these results into the nominal **NOvA** simulation chain to match the **NuMI** neutrino rate [36].

## 1.5 Data Processing and Event Reconstruction

Both data and simulation events for all **NOvA** detectors are passed through the same event reconstruction and particle identification algorithms. The reconstruction was specifically developed with the  $\nu_e$  appearance search in mind, focusing on identifying the  $\nu_e$ **CC** signal against the  $\nu_\mu$ **CC** and Neutral Current (NC) backgrounds. Each **NOvA** detector has to deal with different challenges, with multiple neutrinos interacting during one beam spill in the **ND**, and a large cosmic background in the **FD** [62].

The output from the **DAQ** system for each channel is called a *raw hit*. Hits are grouped into 550  $\mu\text{s}$ -long windows and passed to an offline reconstruction chain [62]. Reconstruction starts by grouping hits into *slices* based on their proximity to other hits in both time and space [63]. Slices are designed to ideally contain only a single neutrino interaction event.

For events that produce hadronic and electromagnetic showers, reconstruction first identifies straight lines through major features using a modified Hough transform [64], representing particle directions. These lines are passed to the Elastic Arms algorithm [65] to identify *vertex* candidates from their intersection points. Hits are then clustered into *prongs*, which are collections of hits with a start point, based on the vertex, and a direction, using a k-means algorithm called FuzzyK [66, 67]. Here ‘fuzzy’ means that each hit can belong to multiple prongs. Prongs are first created separately for each view (also called 2D prongs) and then, if possible, view-matched into 3D prongs (from here on referred to as prongs) [62]. Figure 1.7 shows an example of a simulated electron shower, where the reconstructed vertex is shown as a red cross and the prong as a red shaded area. The prong groups together all the hits that are part of the shower, while removing the background hits, shown in grey.

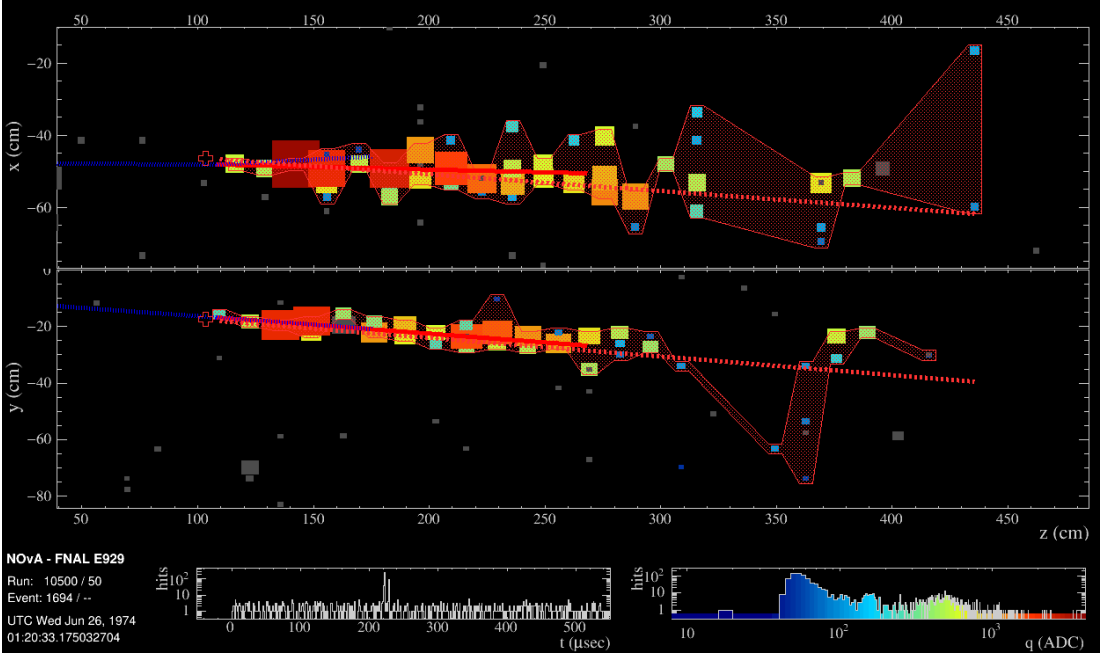


Figure 1.7: Reconstruction of a simulated single electron event in the NOvA ND. The red cross is the reconstructed vertex, the shaded area shows the cluster of hits into a prong and the dotted red line shows the estimated shower direction. The blue dotted line shows the true direct of the scattering neutrino and the solid red line the true momentum of the scattered electron. Figure from internal NOvA database [68].

For particles that are represented by tracks rather than showers (especially muons), the reconstruction takes the slice hits and forms ‘Kalman tracks’ based on a Kalman filter [69]. In addition to the start point and the direction, which exist also for prongs, tracks also contain information on the vector of trajectory points that make up the track and on the end point - and therefore on the track length. A parallel tracking algorithm takes in the Elastic Arms vertex and the Fuzzy-K prongs and forms Break Point Fitter (BPF) tracks [70, 71], using a model of Coulomb scattering and energy loss. BPF tracks also contain an information on the particle 4-momenta based on various particle assumptions, most notably the muon assumption. For cosmic particles, mostly muons, NOvA uses another track reconstruction algorithm, called ‘window cosmic track’ [72]. It uses a sliding 5 plane-long window, in which it fits a straight line to the recorded hits. The window starts from the end of the detector and then slides forward and repeats the fitting process until all hits are processed. This way it accounts for possible Coulomb scattering of cosmic muons. The intersection of each cosmic track with the edge of the detector (or extrapolation of the track to the edge of the detector) is reconstructed as the ‘cosmic ray vertex’.

To identify individual particles and remove backgrounds, **NOvA** uses several Machine Learning (ML) algorithms, outputs of which are used in combination with the information from classical reconstruction algorithms for Particle Identification (PID). The most common topologies for particles interacting in **NOvA** detectors are shown in Fig. 1.8. Muons are easily identifiable as single long tracks which decay into an electron (or positron) if stopping inside of the detector. Both electrons and  $\pi^0$ 's produce electromagnetic showers, but thanks to the low-Z composition and high granularity of the detector, there is a gap between the interaction vertex and the electromagnetic shower for the  $\pi^0$ .

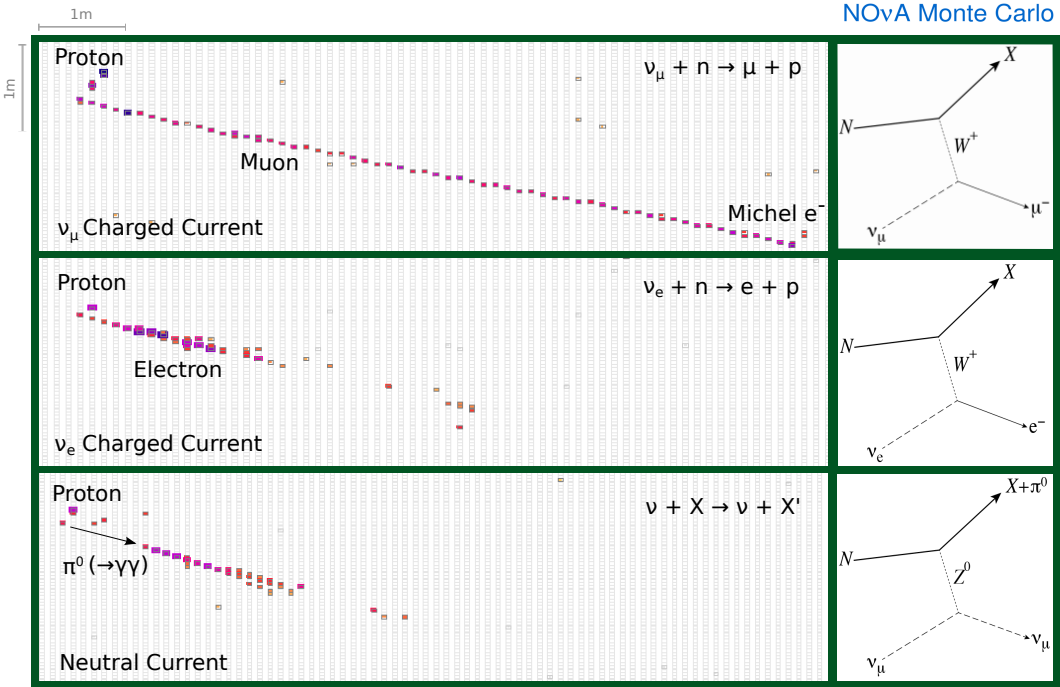


Figure 1.8: Different event topologies as seen in the **NOvA** detectors with corresponding Feynman diagrams [62]. Each event is a simulated 2.15 GeV neutrino interacting in a **NOvA** detector producing a 0.78 GeV proton and a second 1.86 GeV particle depending on the interactions type. The figure shows only one view and the colouring represents the deposited energy.

One of the ML algorithms that NOvA employs is a Convolutional Neural Network (CNN) based on the GoogLeNet [73] architecture named Convolutional Visual Network (CVN) [74]. When it is applied to identify entire events it is called *EventCVN* and uses slice hits to classify interactions into one of the five categories:  $\nu_e$ ,  $\nu_\mu$ ,  $\nu_\tau$ , NC, or cosmic. The same architecture, but applied to the Fuzzy-K prongs, is called *ProngCVN* [75], and is used to identify what particles the prongs most likely corre-

spond to. This assignment is useful in calculation of prong energy, as described in Sec. 1.7. Another [ML](#) algorithm is specifically designed for identifying muons and is based on a Boosted Decision Tree (BDT). It is called Reconstructed Muon Identifier (REMid) [69] and uses the reconstructed Kalman tracks as inputs.

## 1.6 Detector Calibration

The energy deposited within [NOvA](#) detectors is represented by the peak [ADC](#) values for each cell the particle passed through, obtained from the readout electronics, as described in Sec. 1.3. The conversion of the peak [ADC](#) values into physical units of energy requires calibrating the [NOvA](#) detectors [76], while accounting for the attenuation of light along the [WLS](#) fibres, or for differences between individual cells. The purpose of calibration is to calculate a conversion factor from  $\text{ADC} \rightarrow \text{MeV}$  for every part of the detector, so that the same energy deposited anywhere and at any time, is recorded as the same value of the reconstructed energy.

[NOvA](#) uses cosmic ray muons for calibration due to their abundance in the [NOvA](#) detectors and their consistent energy deposition. To calculate the absolute energy scale, [NOvA](#) selects a subsample of muons stopping inside of the detectors when they are almost exactly minimum ionising particles (MIP) and therefore have a well understood energy deposition. The cosmic muons are collected using a periodic trigger with the same length as the beam trigger, whilst removing events with timestamps overlapping with the beam spill window. The simulation of cosmic muons is created using the [CRY](#) [60] [MC](#) generator, as outlined in Sec. 1.4.

Cosmic muon tracks are reconstructed using the window cosmic track algorithm described in Sec. 1.5. The selection of well reconstructed cosmic tracks requires that at least 80% of all hits from the reconstructed slice contribute to the track [29]. Each track must have at least 2 hits in both the x and y views and the difference in the number of planes the track crossed between the views must be at most 10% of the total number of planes. Also, the plane where each track starts or stops in one view must be within 3 planes of the start or stop plane in the other view. Additionally, since tracks that do not cross many planes tend to not be reconstructed very well, the extent of each track in the z direction must be at least 70 cm and tracks must have

at least 20% of their total track direction in the z axis. Tracks with on average more than 6 cells per plane and with path lengths through the cell larger than 10 cm are removed for the same reason. Furthermore, all the reconstructed tracks must start at most 10 cm from the edge inside of the detector and stop at most 10 cm outside of the detector. Lastly, tracks with trajectory points far away from each other are also removed. The selection of stopping muons for the absolute energy scale relies on identifying Michel electrons, which are produced by decaying muons at the end of their tracks, as can be seen on the top panel of Fig. 1.8.

Since the energy deposited in a cell is proportional to the distance the particle travels through the cell, the input variable for calibration is the deposited energy divided by the path length through the cell  $\text{PE}/\text{cm}$ . To ensure the path length is well calculated, all hits used in calibration must satisfy the so-called ‘tricell’ condition, shown in Fig. 1.9. This means that for each calibration hit, there must be a corresponding hit in both of the surrounding cells in the same plane for the same track. The path length can then be calculated simply from the height of the cell and the angle of the reconstructed track. In case there is a bad channel in a neighbouring cell (right side of Fig. 1.9), this channel is ignored and the tricell condition looks one cell further [76]. If the tricell condition fails, the hit can still pass the ‘z tricell’ condition, which is a longitudinal equivalent of the tricell condition and requires a hit in both the neighbouring planes in the same view and with the same cell number. The ‘z tricell’ hits are saved separately and may be used if there are no hits satisfying the original tricell condition. This is especially useful for the cells on the edge of the detector, which fail the tricell condition due to only having one neighbouring cell.

The calibration conversion factor from the signal recorded by the detector readout to the deposited energy can be expressed by as

$$E_{\text{dep}} \text{ [MeV]} = \text{Signal} \text{ [ADC]} \times S_d \times TS_{d,i}^{\text{CALIB}} \times R_{d,i}(t) \times A_d(t). \quad (1.1)$$

The calibration scale therefore consists of four separate and complementary factors: the Scale ( $S_d$ ), the Threshold and Shielding correction ( $TS_{d,i}$ ), the Relative calibration ( $R_{d,i}(t)$ ) and the Absolute calibration ( $A_d(t)$ ), all described below. Each part is calculated for each detector separately, as indicated by the subscript  $d$ . The threshold and shielding correction is only used during calibration and is omitted when apply-

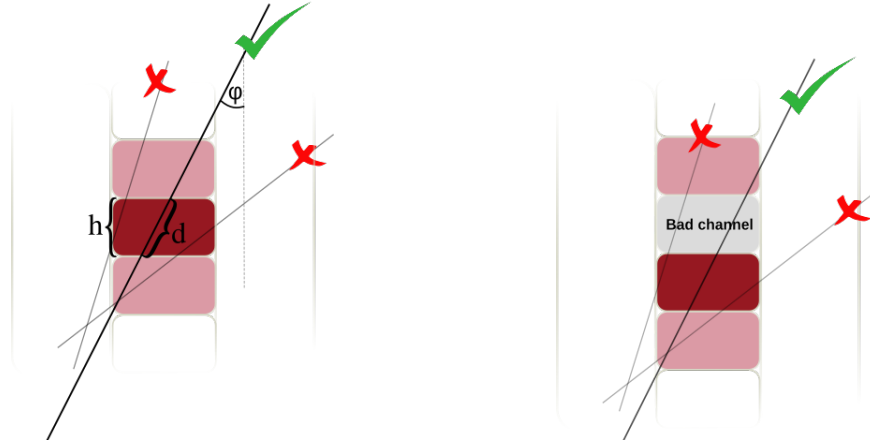


Figure 1.9: Illustration of the tricell condition. Only the hits with two surrounding hits in the same plane are used in the [NOvA](#) calibration, as shown on the left plot. This is to ensure a good quality of the path length ( $d$ ) reconstruction, which is calculated from the known cell height ( $h$ ) and the reconstructed track angle ( $\varphi$ ). In case the hit is next to a bad channel, as shown on the right plot, the bad channel is ignored and the tricell condition requires a hit in the next cell over.

ing the calibration results. The relative and absolute calibrations are calculated for each time period separately to account for possible changes in the energy deposition throughout the time, possibly caused by the ageing of the scintillator oil, or of the readout electronics. The time periods are either determined by a fixed time interval, or by running conditions separated by significant changes to the readout or the [DAQ](#) systems, including the summer shutdown.

The threshold and shielding correction and the relative calibration calculate a calibration factor for each position within the detector to account for variations caused by the attenuation of light as it travels through the [WLS](#) fibres, or by differences between individual cells. This is expressed with a subscript  $i$  in Eq. 1.1. For data, the position of a hit in the detector is described by the plane number, cell number and the position within the cell ( $w$ ).  $w$  is calculated as the projection of the cosmic track to the central cell axis and its value is equivalent to the x axis (y axis) coordinate of the projection for the horizontal (vertical) cells, with the 0 value at the centre of the cell [76].

For simulation, the calibration does not use the plane number to determine the position within a detector, as by construction all detector planes should have the same readout. This significantly reduces the requirements for the number of events that need to be simulated, reconstructed, and calibrated, especially for the [FD](#) with 896

planes. However, in reality there are some variations in the detector response between individual planes, caused by different *brightness* qualities of the fibres, zipped or twisted fibres, different qualities of the scintillator, possible air bubbles, and potentially other factors. To include these differences in simulation without having to simulate every cell individually, all the cells are divided into 12 equally populated Fibre Brightness (FB) bins based on the uncorrected average response in the center of that cell, as shown in Fig. 1.10. These FB bins describe the relative differences in the detector response between individual cells [77].

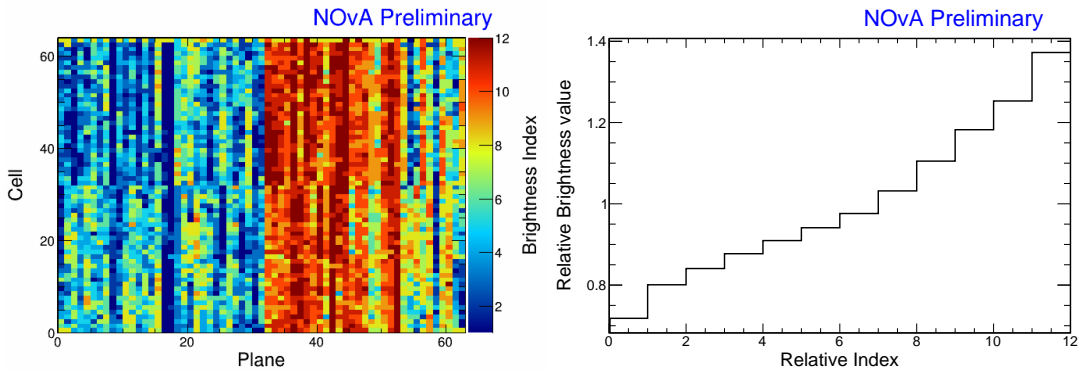


Figure 1.10: Distribution of the NOvA detector cells into 12 brightness bins (left plot), each representing a relative difference in energy response (right plot) due to different brightnesses of the fibres, scintillators, or readout. This is an example from the NOvA Test Beam detector, described in Sec. ??, where the left side of the detector (planes 1-32) has clearly lower response relative to the right side of the detector (planes 33-64).

### 1.6.1 Scale

The scale calibration factor from Eq. 1.1 is a simple conversion from the peak [ADC](#) value into the number of [PEs](#). This factor only depends on the [APD](#) gain (which was different in the beginning of [NOvA](#) data taking) and on the [FEB](#) type (different between detectors, as described in Sec. 1.3).

### 1.6.2 Threshold and Shielding Correction

The threshold and shielding correction accounts for two assumptions, which hold true in most cases in [NOvA](#), but fall short for some hits at the bottom of the detector, or far away from the readout, especially for the [FD](#) [76].

The first assumption is that the [ADC](#) response to the photon signal is linear, which is mostly true except close to the [APD](#) threshold. Energy deposited far away from the

readout may produce photons that get attenuated enough to be shifted below the threshold. However, due to natural fluctuations of the number of photons created by the energy deposition, the same deposited energy may also produce photons that would make it over the threshold, therefore making it appear that the actual deposited energy was higher than in reality, introducing a bias to the calibration. The threshold correction is calculated using simulation, as the ratio between the mean of the Poisson distribution of the true number of the created PE ( $\text{PE}_{Poisson\lambda}$ ) and the number of the ‘reconstructed’ PE seen by the APD ( $\text{PE}_{Reco}$ ).

The second assumption is that the spectrum of cosmic muons is uniform within each detector. Again, this is generally true, but breaks down in the FD, which is big enough for the top of the detector to shield the bottom of the detector and therefore affect the energy distribution. The shielding correction is calculated from simulation as a ratio between the expected deposited energy if the particle was a MIP ( $E_{MIP}$ ), which is estimated from simulation for the NOvA scintillator as  $E_{MIP} = 1.78 \text{ MeV/cm}$  and the true deposited energy ( $E_{true}$ ).

The total threshold and shielding correction is calculated for simulated events in each cell, FB bin and  $w$  as

$$TS_i = \frac{\text{PE}_{Poisson\lambda}}{\text{PE}_{Reco}} \frac{E_{MIP}}{E_{True}}. \quad (1.2)$$

To ensure that the correction changes smoothly across each cell position, the final correction is calculated as a fit to the mean correction value along  $w$  in each cell and FB bin.

### 1.6.3 Relative Calibration

The main goal of the relative calibration is to correct for the attenuation of the scintillator light as it travels through the WLS fibre to the readout. The attenuation in each cell is estimated by performing an ‘attenuation fit’ to the mean response in PE/cm, as shown in Fig. 1.11. The relative calibration scale is then calculated as the ratio between the average response in PE/cm across the entire detector (can differ between detectors) and the result of the attenuation fit in each particular position within the detector. The response after applying the relative calibration scale is expressed as Cor-

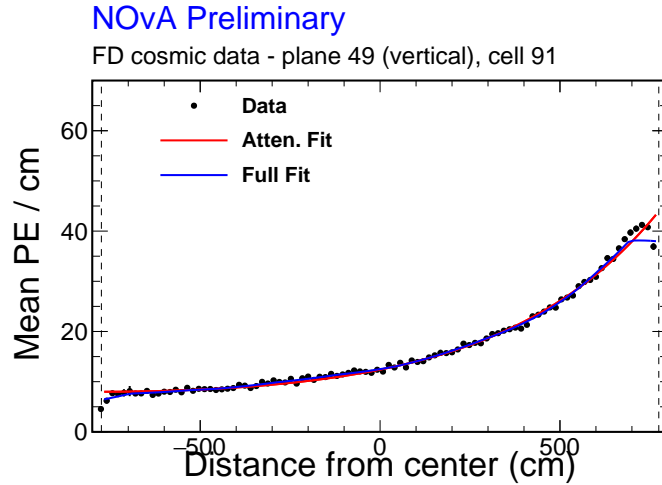


Figure 1.11: Example attenuation fit for a single cell in the NOvA FD across its full length, as shown by dashed vertical lines. The red line shows the initial exponential fit and the blue line shows the full fit after the LOWESS correction, both described in text. Figure from [78].

rected Photo Electrons (PECorrs). Since the relative calibration scale is calculated for each cell independently, it effectively corrects for the relative differences between detector cells as well as for the attenuation. Therefore, the resulting distribution of PE<sub>corr</sub>/cm should be uniform across the detector, especially along the plane, cell and  $w$  [76].

The first step to do the attenuation fit is to create ‘attenuation profiles’ for each cell. Attenuation profiles are profile histograms of mean detector response over the path length through the cell, in the units of PE/cm, along the position within the cell. An example attenuation profile is shown in Fig. 1.11 as black dots. The threshold and shielding correction described in Sec. 1.6.2 is applied to the attenuation profiles before doing the attenuation fit, which consists of two steps.

1. The first step is a three-parameter exponential fit according to

$$y = C + A \left( \exp \left( \frac{w}{X} \right) + \exp \left( -\frac{L+w}{X} \right) \right), \quad (1.3)$$

where  $y$  is the fitted response,  $L$  is the length of the cell and  $C$ ,  $A$  and  $X$  are the fitted parameters representing the background, attenuation scale and attenuation length respectively. An example of the exponential fit is shown as a red curve in Fig. 1.11.

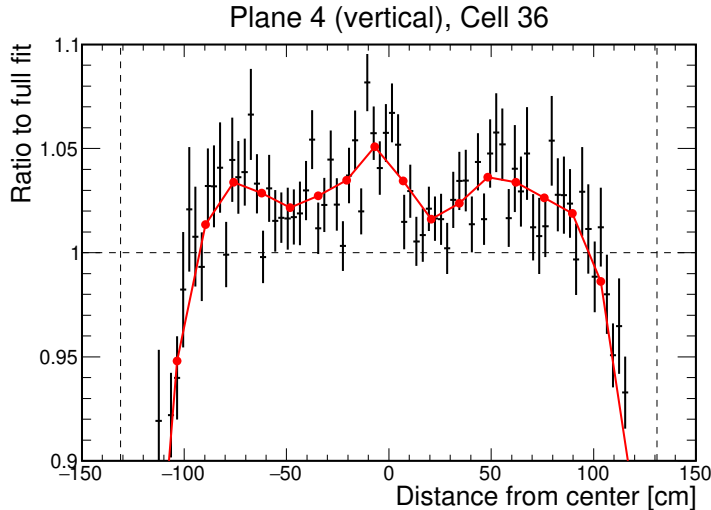


Figure 1.12: Example [LOWESS](#) correction for the residual differences after the exponential part of the attenuation fit of the [NOvA](#) relative calibration. This is an example for a single cell in the [NOvA](#) Test Beam detector with black points showing the residual differences and red line the [LOWESS](#) correction, both described in text.

2. The second step is the smoothing out of residual differences between the exponential fit and the original distribution with the Locally Weighted Scatter plot Smoothing (LOWESS) method, shown in Fig. 1.12. The residual differences get evened out by creating a smooth distribution of 20 locally weighted points across the length of each cell. The result of the [LOWESS](#) correction is then combined with the exponential fit into the full attenuation fit, shown as a blue line in Fig. 1.11.

Even after applying the [LOWESS](#) correction, there are sometimes large differences between the attenuation fit and the fitted response. This is usually caused by a small number of events in that cell, common for cells at the edge of the detector. To ensure a good quality of the attenuation fit, the total  $\chi^2$  between the attenuation fit and the fitted response is calculated and only cells with the final  $\chi^2 \leq 0.2$  are counted as *calibrated*. Cells with  $\chi^2 > 0.2$  are ignored in further processing and marked as *uncalibrated*.

#### 1.6.4 Absolute Calibration

The absolute calibration only uses hits from muons stopping inside of the detector, in a track window 1 – 2 m from the end of their tracks. This is when they are approximately [MIP](#) and their energy deposition is well understood. Additionally, hits at the

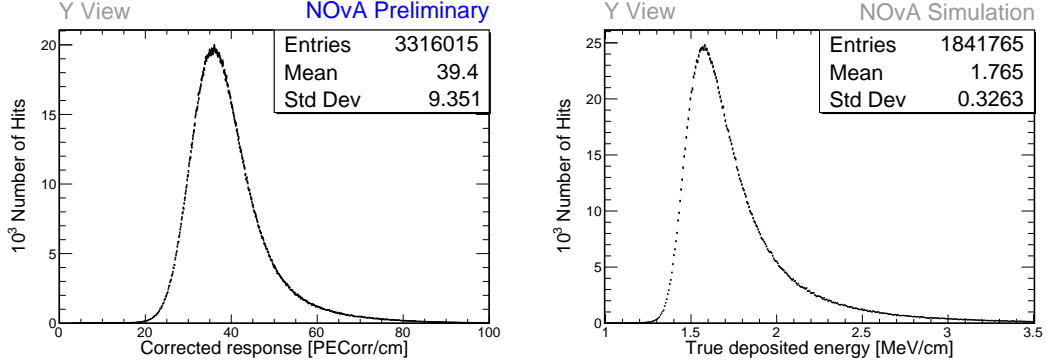


Figure 1.13: The absolute energy scale is calculated as the ratio between the simulated mean true deposited energy (right) and the mean reconstructed energy response (left) for selected stopping muons in each view and each data period or simulation.

edges of each cell are removed to mitigate the effects at the end of the [WLS](#) fibres and the lower number of events at the edge of the detector [29].

First, the relative calibration results are applied to the selected stopping muon hits to get a distribution of the corrected detector response in [PECORR/cm](#), as shown on the left of Fig. 1.13. The mean of this distribution is called the *reconstructed Muon Energy Unit* ([MEU](#)) and is calculated separately in each of the two views, and in each time period or version of simulation. Analogously, the mean of the true deposited energy in [MeV/cm](#) from simulation, shown on the right of Fig. 1.13, is called the *true MEU*. The absolute energy scale (the absolute calibration scale) is then the ratio between the true and the reconstructed [MEU](#) value, where both the [MEU](#) values are taken as a simple average over the two views

$$\text{Absolute Energy Scale} = \frac{\text{MEU}_{\text{True}} \text{ [MeV/cm]}}{\text{MEU}_{\text{Reco}} \text{ [PECORR/cm]}}. \quad (1.4)$$

The values of the absolute energy scales for each data period and simulation, as well as the results of the attenuation fit, are saved in a set of lookup tables, which are then used any time a hit is recorded in the [NOvA](#) detector and processed and reconstructed with the [NOvA](#) algorithms described above.

## 1.7 Energy Estimation

The deposited energy from detector calibration (Sec. 1.6) is only the first step in estimating the neutrino energy ( $E_\nu$ ) required for the main [NOvA](#) analyses.

For the  $\nu_\mu$  disappearance analysis, the  $\nu_\mu$  energy is measured as the sum of the muon energy and the energy of the hadronic shower [7]. The muon energy is identified from the length of its track, without the need of the calibration results. The energy of the hadronic shower is estimated from simulation as a fit to the 2D distribution of the true  $\nu_\mu$  energy minus the reconstructed muon energy, versus the visible (not corrected for the dead material) deposited energy of the hadronic system [75].

For the  $\nu_e$  appearance analysis, the  $\nu_e$  energy is calculated using a quartic fit to the 2D distribution of the electromagnetic versus the hadronic calorimetric energies, both corrected for the energy deposition in the dead material (PVC cells) [75]. The dead material correction is currently just a simple scaling of the deposited energy from calibration for all particles and is calculated from the measurement of the  $\pi^0$  mass peak in the [NOvA ND](#). This correction is correct only for electromagnetic showers and is not directly applicable to hadronic showers. The fit to determine the  $\nu_e$  energy keeps the normalization of both the electromagnetic and the hadronic energies free, so the exact value of the dead material correction is not important. It is however used in other, non-neutrino oscillation analyses.

## 1.8 Systematic Uncertainties at NOvA

Systematic uncertainties in [NOvA](#) analyses arise from the imperfect knowledge on the individual components of the [NOvA](#) experiment, or from the known shortcomings of the prediction used to extract the measured parameters. Even though different analyses in [NOvA](#) need to consider different systematic uncertainties and their effect on the results varies, there are a few commonalities across all [NOvA](#) analyses that are explained below.

Both the 3-flavour [7] and the sterile neutrino [13] oscillation analyses in [NOvA](#) use the [ND](#) to constrain the [FD](#) prediction, which significantly reduces the effect of the neutrino beam and interaction prediction systematic uncertainties. On the other hand, these are the leading sources of systematic uncertainties for the [ND](#)-only analyses, such as the cross section analyses [8–11]. The leading systematic uncertainty for the neutrino oscillation measurements comes from the detector calibration uncertainty. Significant uncertainties for all [NOvA](#) measurements also come from the

neutron modelling, the detector simulation and the muon energy estimation. There are other sources of systematic uncertainties that are not mentioned here as they are sub-dominant, or specific to a certain analysis.

The systematic uncertainty on the prediction of the neutrino beam consists of two parts: the hadron production and the beam focusing uncertainties [36]. The uncertainty for hadron production is estimated by the **PPFX** (describe in Sec. 1.4) using the multi-universe technique. Here we create 100 **PPFX** universes in which the inputs from the external measurements used to constrain the hadron production are randomly floated around their central values within their respective systematic uncertainties. Parts of the hadron production that are not constrained by external measurements are given a conservatively large systematic uncertainty. The beam focusing systematic uncertainties account for the uncertainties on the horn and target positions, the horn current, the beam position on the target, the beam spot size, and the effect of Earth's magnetic field in the beam pipe. **TO DO: Describe the beam PCA and how can we limit the beam uncertainty**

**TO DO: Describe the neutrino interaction modelling systematic uncertainties**

**TO DO: Describe the detector modelling systematic uncertainties** COMMENT: I should probably only discuss the new light level and cherenkov systematic uncertainties from the 3fl technote. This have not been published anywhere yet, but this is what I'm using for the mag. moment analysis

**TO DO: Describe the neutron uncertainty - why do we need it?** COMMENT: Should I describe MENATE or MCNP? Do I even need this here? Not sure if I'm including this in the mag. moment yet. Maybe add it only if I do...

**TO DO: Describe the calibration uncertainties**

**TO DO: Describe the muon energy scale uncertainty - if needed, maybe just briefly...**



# Acronyms

**2P2H** two particle - two hole. 9

**ADC** Analog-to-Digital Converter. 7, 14, 17

**APD** Avalanche Photodiode. 5–7, 10, 17, 18

**ASIC** Application-Specific Integrated Circuit. 6, 7

**BDT** Boosted Decision Tree. 14

**BPF** Break Point Fitter. 12

**CC** Charged current. 9–11

**CMC** Comprehensive Model Configuration. 10

**CNN** Convolutional Neural Network. 13

**COH $\pi$**  Coherent pion production. 9, 10

**CP** Charge conjugation - Parity (symmetry). 1

**CRY** Cosmic-Ray Shower Generator. 10, 14

**CVN** Convolutional Visual Network. 13

**DAQ** Data Acquisition. 6, 11, 16

**DCM** Data Concentration Module. 7

**DIS** Deep Inelastic Scattering. 9, 10

**DUNE** Deep Underground Neutrino Experiment. 1, 9

**FB** Fibre Brightness. 17, 18

**FD** Far Detector. 3–7, 10, 11, 16–19, 22

**FEB** Front End Board. 6, 7, 17

**FERMILAB** Fermi National Accelerator Laboratory. 1, 3, 9

**FHC** Forward Horn Current (neutrino mode). [2](#), [3](#)

**FPGA** Field Programmable Gate Array. [7](#)

**FSI** Final State Interaction. [9](#), [10](#)

**LOWESS** Locally Weighted Scatter plot Smoothing. [19](#), [20](#)

**MC** Monte Carlo. [8–10](#), [14](#)

**MEC** Meson Exchange Current. [9](#), [10](#)

**MEU** Muon Energy Unit. [21](#)

**MI** Main Injector. [1](#), [2](#), [8](#)

**MIP** minimum ionising particles. [14](#), [18](#), [20](#)

**MIPP** Main Injector Particle Production. [9](#)

**ML** Machine Learning. [13](#), [14](#)

**NC** Neutral Current. [11](#), [13](#)

**ND** Near Detector. [1](#), [3–5](#), [7](#), [10–12](#), [22](#)

**NDOS** Near Detector on the Surface. [3](#)

**NOvA** NuMI Off-axis  $\nu_e$  Appearance (experiment). [1](#), [3–14](#), [16–22](#)

**NuMI** Neutrinos from the Main Injector. [1–3](#), [8](#), [9](#), [11](#)

**PE** Photo Electron. [6](#), [7](#), [15](#), [17–19](#)

**PECorr** Corrected Photo Electrons. [18](#), [19](#), [21](#)

**PID** Particle Identification. [13](#)

**POT** Protons On Target. [2](#)

**PPFX** Package to Predict the Flux. [9](#), [23](#)

**PVC** Polyvinyl chloride. [4–6](#), [22](#)

**QE** Quasi Elastic (interaction). [9](#), [10](#)

**REMIN** Reconstructed Muon Identifier. [14](#)

**RES** Resonant baryon production. [9](#), [10](#)

**RHC** Reverse Horn Current (antineutrino mode). [2](#), [3](#)

**WLS** Wavelength Shifting (fibre). [5](#), [6](#), [10](#), [14](#), [16](#), [18](#), [21](#)

# Bibliography

- [1] Nova experiments official website. URL <https://novaexperiment.fnal.gov>. Cited February 2024.
- [2] Fermi national accelerator laboratory official website. URL <https://fnal.gov>. Cited February 2024.
- [3] Gary Feldman for the NOvA Collaboration. Physics of the nova experiment. White paper, 2012. URL <https://nova-docdb.fnal.gov/cgi-bin>ShowDocument?docid=7733>. Public NOvA document: NOVA-doc-7733-v1, cited on 05.2020.
- [4] R.B. Patterson. The NOvA Experiment: Status and Outlook. *Nucl. Phys. B Proc. Suppl.*, 235-236:151–157, 2013. doi:[10.1016/j.nuclphysbps.2013.04.005](https://doi.org/10.1016/j.nuclphysbps.2013.04.005).
- [5] P. Adamson et al. First measurement of muon-neutrino disappearance in NOvA. *Phys. Rev. D*, 93(5):051104, 2016. doi:[10.1103/PhysRevD.93.051104](https://doi.org/10.1103/PhysRevD.93.051104).
- [6] M.A. Acero et al. First Measurement of Neutrino Oscillation Parameters using Neutrinos and Antineutrinos by NOvA. *Phys. Rev. Lett.*, 123(15):151803, 2019. doi:[10.1103/PhysRevLett.123.151803](https://doi.org/10.1103/PhysRevLett.123.151803).
- [7] M. A. Acero et al. Improved measurement of neutrino oscillation parameters by the NOvA experiment. *Phys. Rev. D*, 106(3):032004, 2022. doi:[10.1103/PhysRevD.106.032004](https://doi.org/10.1103/PhysRevD.106.032004).
- [8] M. A. Acero et al. Measurement of neutrino-induced neutral-current coherent  $\pi^0$  production in the NOvA near detector. *Phys. Rev. D*, 102(1):012004, 2020. doi:[10.1103/PhysRevD.102.012004](https://doi.org/10.1103/PhysRevD.102.012004).
- [9] M. A. Acero et al. Measurement of the double-differential muon-neutrino charged-current inclusive cross section in the NOvA near detector. *Phys. Rev. D*, 107(5):052011, 2023. doi:[10.1103/PhysRevD.107.052011](https://doi.org/10.1103/PhysRevD.107.052011).
- [10] M. A. Acero et al. Measurement of the  $\nu_e$ –Nucleus Charged-Current Double-Differential Cross Section at  $\langle E_\nu \rangle = 2.4$  GeV using NOvA. *Phys. Rev. Lett.*, 130(5):051802, 2023. doi:[10.1103/PhysRevLett.130.051802](https://doi.org/10.1103/PhysRevLett.130.051802).

- [11] M. A. Acero et al. Measurement of  $\nu_\mu$  charged-current inclusive  $\pi^0$  production in the NOvA near detector. *Phys. Rev. D*, 107(11):112008, 2023. doi:[10.1103/PhysRevD.107.112008](https://doi.org/10.1103/PhysRevD.107.112008).
- [12] P. Adamson et al. Search for active-sterile neutrino mixing using neutral-current interactions in NOvA. *Phys. Rev. D*, 96(7):072006, 2017. doi:[10.1103/PhysRevD.96.072006](https://doi.org/10.1103/PhysRevD.96.072006).
- [13] M. A. Acero et al. Search for Active-Sterile Antineutrino Mixing Using Neutral-Current Interactions with the NOvA Experiment. *Phys. Rev. Lett.*, 127(20):201801, 2021. doi:[10.1103/PhysRevLett.127.201801](https://doi.org/10.1103/PhysRevLett.127.201801).
- [14] M. A. Acero et al. Supernova neutrino detection in NOvA. *JCAP*, 10:014, 2020. doi:[10.1088/1475-7516/2020/10/014](https://doi.org/10.1088/1475-7516/2020/10/014).
- [15] M. A. Acero et al. Extended search for supernovalike neutrinos in NOvA coincident with LIGO/Virgo detections. *Phys. Rev. D*, 104(6):063024, 2021. doi:[10.1103/PhysRevD.104.063024](https://doi.org/10.1103/PhysRevD.104.063024).
- [16] M. A. Acero et al. Search for slow magnetic monopoles with the NOvA detector on the surface. *Phys. Rev. D*, 103(1):012007, 2021. doi:[10.1103/PhysRevD.103.012007](https://doi.org/10.1103/PhysRevD.103.012007).
- [17] Peter N. Shanahan and Patricia LaVern Vahle. Physics with NOvA: a half-time review. *Eur. Phys. J. ST*, 230(24):4259–4273, 2021. doi:[10.1140/epjs/s11734-021-00285-9](https://doi.org/10.1140/epjs/s11734-021-00285-9).
- [18] Peter Shanahan and Patricia Vahle. The NOvA Physics Program through 2025. Snowmass 2021 Letters of Interest NF, 135. URL [https://www.snowmass21.org/docs/files/summaries/NF/SNOWMASS21-NF1\\_NF3\\_Patricia\\_Vahle-145.pdf](https://www.snowmass21.org/docs/files/summaries/NF/SNOWMASS21-NF1_NF3_Patricia_Vahle-145.pdf).
- [19] P. Adamson et al. The NuMI Neutrino Beam. *Nucl. Instrum. Meth. A*, 806:279–306, 2016. doi:[10.1016/j.nima.2015.08.063](https://doi.org/10.1016/j.nima.2015.08.063).
- [20] Records. URL <https://operations.fnal.gov/records/>. Performance records achieved by the Fermilab accelerators. Cited May 2024.

- [21] Katsuya Yonehara. Megawatt upgrade of numi target system. 1 2022. URL <https://www.osti.gov/biblio/1844332>.
- [22] Leonidas Aliaga Soplin. *Neutrino Flux Prediction for the NuMI Beamline*. PhD thesis, William-Mary Coll., 2016.
- [23] Leonidas Aliaga Soplin. 2017-2018 Beam Plots. NOVA Document 20843. URL <https://nova-docdb.fnal.gov/cgi-bin/sso>ShowDocument?docid=20843>. NOvA internal document.
- [24] D. S. Ayres et al. The nova technical design report. *NOvA Collaboration*, 2007. doi:[10.2172/935497](https://doi.org/10.2172/935497).
- [25] Yury Kudenko. Neutrino detectors for oscillation experiments. *JINST*, 12(06):C06003, 2017. doi:[10.1088/1748-0221/12/06/C06003](https://doi.org/10.1088/1748-0221/12/06/C06003).
- [26] S. Mufson et al. Liquid scintillator production for the NOvA experiment. *Nucl. Instrum. Meth. A*, 799:1–9, 2015. doi:[10.1016/j.nima.2015.07.026](https://doi.org/10.1016/j.nima.2015.07.026).
- [27] Alex Sousa. Density of NOvA Liquid Scintillator at 69° F. NOVA Document 11886. URL <https://nova-docdb.fnal.gov/cgi-bin/sso>ShowDocument?docid=11886>. NOvA internal document.
- [28] M.J. Berger, J.S. Coursey, M.A. Zucker, and J. Chang. ESTAR, PSTAR, and ASTAR: Computer Programs for Calculating Stopping-Power and Range Tables for Electrons, Protons, and Helium Ions (version 1.2.3). URL <http://physics.nist.gov/Star>.
- [29] Luke Vinton. Calorimetric Energy Scale Calibration of the NOvA Detectors. NOVA Document 13579, document FA\_Calorimetric\_energy\_scale.pdf. URL <https://nova-docdb.fnal.gov/cgi-bin/sso>ShowDocument?docid=13579>. NOvA Technical Note.
- [30] Xinchun Tian. NOvA Data Acquisition Software System. In *Meeting of the APS Division of Particles and Fields*, 9 2011.
- [31] Joao Coelho, Barnali Chowdhury, and Ryan Murphy. Tech note: Good data selection. NOVA Document 13546. URL <https://nova-docdb.fnal.gov/cgi-bin/sso>ShowDocument?docid=13546>. NOvA technical note.

- [32] Jonathan M. Paley. BadChannels Technical Note. NOVA Document 12771. URL <https://nova-docdb.fnal.gov/cgi-bin/sso>ShowDocument?docid=12771>. NOvA technical note.
- [33] A. Aurisano, C. Backhouse, R. Hatcher, N. Mayer, J. Musser, R. Patterson, R. Schroeter, and A. Sousa. The NOvA simulation chain. *J. Phys. Conf. Ser.*, 664(7):072002, 2015. doi:[10.1088/1742-6596/664/7/072002](https://doi.org/10.1088/1742-6596/664/7/072002).
- [34] S. Agostinelli et al. GEANT4—a simulation toolkit. *Nucl. Instrum. Meth. A*, 506: 250–303, 2003. doi:[10.1016/S0168-9002\(03\)01368-8](https://doi.org/10.1016/S0168-9002(03)01368-8).
- [35] Zarko Pavlovic. *Observation of Disappearance of Muon Neutrinos in the NuMI Beam*. PhD thesis, Texas U., 2008.
- [36] L. Aliaga et al. Neutrino Flux Predictions for the NuMI Beam. *Phys. Rev. D*, 94(9):092005, 2016. doi:[10.1103/PhysRevD.94.092005](https://doi.org/10.1103/PhysRevD.94.092005). [Addendum: *Phys.Rev.D* 95, 039903 (2017)].
- [37] C. Alt et al. Inclusive production of charged pions in p+C collisions at 158-GeV/c beam momentum. *Eur. Phys. J. C*, 49:897–917, 2007. doi:[10.1140/epjc/s10052-006-0165-7](https://doi.org/10.1140/epjc/s10052-006-0165-7).
- [38] Gemma Maria Tinti. *Sterile neutrino oscillations in MINOS and hadron production in pC collisions*. PhD thesis, 2010.
- [39] B Baatar, G Barr, J Bartke, L Betev, O Chvala, J Dolejsi, V Eckardt, HG Fischer, Z Fodor, A Karev, et al. Inclusive production of protons, anti-protons, neutrons, deuterons and tritons in p+ c collisions at 158 gev/c beam momentum. *The European Physical Journal C*, 73:1–66, 2013. doi:[10.1140/epjc/s10052-013-2364-3](https://doi.org/10.1140/epjc/s10052-013-2364-3).
- [40] D. S. Barton et al. Experimental study of the  $a$  dependence of inclusive hadron fragmentation. *Phys. Rev. D*, 27:2580–2599, Jun 1983. doi:[10.1103/PhysRevD.27.2580](https://doi.org/10.1103/PhysRevD.27.2580).
- [41] Andrey V. Lebedev. *Ratio of Pion Kaon Production in Proton Carbon Interactions*. PhD thesis, 2007.

- [42] T.T. Böhlen, F. Cerutti, M.P.W. Chin, A. Fassò, A. Ferrari, P.G. Ortega, A. Mairani, P.R. Sala, G. Smirnov, and V. Vlachoudis. The fluka code: Developments and challenges for high energy and medical applications. 120:211–214. ISSN 0090-3752. doi:[10.1016/j.nds.2014.07.049](https://doi.org/10.1016/j.nds.2014.07.049).
- [43] Alfredo Ferrari, Paola R. Sala, Alberto Fasso, and Johannes Ranft. FLUKA: A multi-particle transport code (Program version 2005). 10 2005. doi:[10.2172/877507](https://doi.org/10.2172/877507).
- [44] A. Aduszkiewicz et al. Measurements of production and inelastic cross sections for p+C , p+Be , and p+Al at 60 GeV/c and p+C and p+Be at 120 GeV/c. *Phys. Rev. D*, 100(11):112001, 2019. doi:[10.1103/PhysRevD.100.112001](https://doi.org/10.1103/PhysRevD.100.112001).
- [45] H. Adhikary et al. Measurements of  $\pi^+$ ,  $\pi^-$ ,  $p$ ,  $\bar{p}$ ,  $K^+$  and  $K^-$  production in 120 GeV/c p + C interactions. *Phys. Rev. D*, 108:072013, 2023. doi:[10.1103/PhysRevD.108.072013](https://doi.org/10.1103/PhysRevD.108.072013).
- [46] H. Adhikary et al. Measurements of KS0,  $\Lambda$ , and  $\Lambda^-$  production in 120 GeV/c p+C interactions. *Phys. Rev. D*, 107(7):072004, 2023. doi:[10.1103/PhysRevD.107.072004](https://doi.org/10.1103/PhysRevD.107.072004).
- [47] A. Aduszkiewicz et al. Measurements of hadron production in  $\pi^+ + C$  and  $\pi^+ + Be$  interactions at 60 GeV/c. *Phys. Rev. D*, 100(11):112004, 2019. doi:[10.1103/PhysRevD.100.112004](https://doi.org/10.1103/PhysRevD.100.112004).
- [48] Matej Pavin. Hadron production measurements for neutrino experiments, 2020. URL [https://indico.fnal.gov/event/43209/contributions/187869/attachments/130502/159028/HadronProduction\\_neutrino2020.pdf](https://indico.fnal.gov/event/43209/contributions/187869/attachments/130502/159028/HadronProduction_neutrino2020.pdf). Presented on Neutrino 2020 conference.
- [49] T. Akaishi et al. EMPHATIC: A Proposed Experiment to Measure Hadron Scattering and Production Cross Sections for Improved Neutrino Flux Predictions. 12 2019.
- [50] C. Andreopoulos et al. The GENIE Neutrino Monte Carlo Generator. *Nucl. Instrum. Meth. A*, 614:87–104, 2010. doi:[10.1016/j.nima.2009.12.009](https://doi.org/10.1016/j.nima.2009.12.009).

- [51] J. Nieves, J. E. Amaro, and M. Valverde. Inclusive quasielastic charged-current neutrino-nucleus reactions. *Phys. Rev. C*, 70:055503, Nov 2004. doi:[10.1103/PhysRevC.70.055503](https://doi.org/10.1103/PhysRevC.70.055503).
- [52] Aaron S. Meyer, Minerba Betancourt, Richard Gran, and Richard J. Hill. Deuterium target data for precision neutrino-nucleus cross sections. *Phys. Rev. D*, 93:113015, Jun 2016. doi:[10.1103/PhysRevD.93.113015](https://doi.org/10.1103/PhysRevD.93.113015).
- [53] J. Nieves, I. Ruiz Simo, and M. J. Vicente Vacas. Inclusive charged-current neutrino-nucleus reactions. *Phys. Rev. C*, 83:045501, Apr 2011. doi:[10.1103/PhysRevC.83.045501](https://doi.org/10.1103/PhysRevC.83.045501).
- [54] R. Gran, J. Nieves, F. Sanchez, and M. J. Vicente Vacas. Neutrino-nucleus quasielastic and 2p2h interactions up to 10 gev. *Phys. Rev. D*, 88:113007, Dec 2013. doi:[10.1103/PhysRevD.88.113007](https://doi.org/10.1103/PhysRevD.88.113007).
- [55] Ch. Berger and L. M. Sehgal. Lepton mass effects in single pion production by neutrinos. *Phys. Rev. D*, 76:113004, Dec 2007. doi:[10.1103/PhysRevD.76.113004](https://doi.org/10.1103/PhysRevD.76.113004).
- [56] Ch. Berger and L. M. Sehgal. Partially conserved axial vector current and coherent pion production by low energy neutrinos. *Phys. Rev. D*, 79:053003, Mar 2009. doi:[10.1103/PhysRevD.79.053003](https://doi.org/10.1103/PhysRevD.79.053003).
- [57] A Bodek and U. K. Yang. Higher twist, xi(omega) scaling, and effective LO PDFs for lepton scattering in the few GeV region. *J. Phys. G*, 29:1899–1906, 2003. doi:[10.1088/0954-3899/29/8/369](https://doi.org/10.1088/0954-3899/29/8/369).
- [58] T. Yang, C. Andreopoulos, H. Gallagher, K. Hoffmann, and P. Kehayias. A Hadronization Model for Few-GeV Neutrino Interactions. *Eur. Phys. J. C*, 63: 1–10, 2009. doi:[10.1140/epjc/s10052-009-1094-z](https://doi.org/10.1140/epjc/s10052-009-1094-z).
- [59] L.L. Salcedo, E. Oset, M.J. Vicente-Vacas, and C. Garcia-Recio. Computer simulation of inclusive pion nuclear reactions. 484(3):557–592. ISSN 0375-9474. doi:[10.1016/0375-9474\(88\)90310-7](https://doi.org/10.1016/0375-9474(88)90310-7).
- [60] Chris Hagmann, David Lange, and Douglas Wright. Cosmic-ray shower generator (cry) for monte carlo transport codes. volume 2, pages 1143 – 1146. ISBN 978-1-4244-0922-8. doi:[10.1109/NSSMIC.2007.4437209](https://doi.org/10.1109/NSSMIC.2007.4437209).

- [61] C. N. Chou. The nature of the saturation effect of fluorescent scintillators. *Phys. Rev.*, 87:904–905, Sep 1952. doi:[10.1103/PhysRev.87.904](https://doi.org/10.1103/PhysRev.87.904). URL <https://link.aps.org/doi/10.1103/PhysRev.87.904>.
- [62] M. Baird, J. Bian, M. Messier, E. Niner, D. Rocco, and K. Sachdev. Event Reconstruction Techniques in NOvA. *J. Phys. Conf. Ser.*, 664(7):072035, 2015. doi:[10.1088/1742-6596/664/7/072035](https://doi.org/10.1088/1742-6596/664/7/072035).
- [63] Martin Ester, Hans-Peter Kriegel, Jörg Sander, and Xiaowei Xu. A density-based algorithm for discovering clusters in large spatial databases with noise. In *Proceedings of the Second International Conference on Knowledge Discovery and Data Mining*, KDD’96, page 226–231. AAAI Press, 1996. doi:[10.5555/3001460.3001507](https://doi.org/10.5555/3001460.3001507).
- [64] Leandro A. F. Fernandes and Manuel Menezes de Oliveira Neto. Real-time line detection through an improved hough transform voting scheme. *Pattern Recognit.*, 41:299–314, 2008. doi:[10.1016/j.patcog.2007.04.003](https://doi.org/10.1016/j.patcog.2007.04.003). URL <https://api.semanticscholar.org/CorpusID:5996185>.
- [65] Mattias Ohlsson, Carsten Peterson, and Alan L. Yuille. Track finding with deformable templates – the elastic arms approach. 71(1):77–98. ISSN 0010-4655. doi:[10.1016/0010-4655\(92\)90074-9](https://doi.org/10.1016/0010-4655(92)90074-9). URL <https://www.sciencedirect.com/science/article/pii/0010465592900749>.
- [66] R. Krishnapuram and J.M. Keller. A possibilistic approach to clustering. *IEEE Transactions on Fuzzy Systems*, 1(2):98–110, 1993. doi:[10.1109/91.227387](https://doi.org/10.1109/91.227387).
- [67] Miin-Shen Yang and Kuo-Lung Wu. Unsupervised possibilistic clustering. 39(1):5–21. ISSN 0031-3203. doi:<https://doi.org/10.1016/j.patcog.2005.07.005>. URL <https://www.sciencedirect.com/science/article/pii/S0031320305002943>.
- [68] Jianming Bian, Hongyue Duyang, and Alexander Radovic. Blessing package for Neutrino-Electron Scattering and Coherent Pi0. NOVA Document 13862. URL <https://nova-docdb.fnal.gov/cgi-bin/sso>ShowDocument?docid=13862>. NOvA internal document.
- [69] Nicholas Jacob Raddatz. *Measurement of Muon Neutrino Disappearance with Non-Fiducial Interactions in the NOvA Experiment*. PhD thesis, Minnesota U., 2016.

- [70] Michael David Baird. *An Analysis of Muon Neutrino Disappearance from the NuMI Beam Using an Optimal Track Fitter*. PhD thesis, Indiana U., 2015.
- [71] G. Lutz. Optimum track fitting in the presence of multiple scattering. 273(1):349–361. ISSN 0168-9002. doi:[https://doi.org/10.1016/0168-9002\(88\)90836-4](https://doi.org/10.1016/0168-9002(88)90836-4). URL <https://www.sciencedirect.com/science/article/pii/0168900288908364>.
- [72] Brian Rebel. Window tracking algorithm for cosmic ray muons. NOVA Document 15977-v1. URL <https://nova-docdb.fnal.gov/cgi-bin/sso>ShowDocument?docid=15977>. NOvA internal document.
- [73] Christian Szegedy, Wei Liu, Yangqing Jia, Pierre Sermanet, Scott Reed, Dragomir Anguelov, Dumitru Erhan, Vincent Vanhoucke, and Andrew Rabinovich. Going Deeper with Convolutions. art. arXiv:1409.4842. doi:[10.48550/arXiv.1409.4842](https://arxiv.org/abs/1409.4842).
- [74] A. Aurisano, A. Radovic, D. Rocco, A. Himmel, M.D. Messier, E. Niner, G. Pawloski, F. Psihas, A. Sousa, and P. Vahle. A Convolutional Neural Network Neutrino Event Classifier. *JINST*, 11(09):P09001, 2016. doi:[10.1088/1748-0221/11/09/P09001](https://doi.org/10.1088/1748-0221/11/09/P09001).
- [75] Fernanda Psihas. Measurement of long baseline neutrino oscillations and improvements from deep learning. 1 2018. doi:[10.2172/1437288](https://doi.org/10.2172/1437288). URL <https://www.osti.gov/biblio/1437288>.
- [76] Prabhjot Singh. *Extraction of Neutrino Oscillation Parameters using a Simultaneous Fit of  $\nu_\mu$  Disappearance and  $\nu_e$  Appearance data with the NOvA Experiment*. PhD thesis, University of Delhi, Dept. of Physics and Astrophysics, India, Delhi U., 9 2019.
- [77] Ryan J. Nichol. Fibre brightness from cosmic muon data. NOVA Document 34909. URL <https://nova-docdb.fnal.gov/cgi-bin/sso>ShowDocument?docid=34909>. NOvA technical note.
- [78] Prabhjot Singh. Attenuation Calibration of the NOvA Detectors. In *The 38th International Conference on High Energy Physics (ICHEP 2016)*, 2024. URL <https://nova-docdb.fnal.gov/cgi-bin/sso>ShowDocument?docid=15840>. (cited on 03.2024).